

High-resolution observations of the solar photosphere, chromosphere and transition region

A database of coordinated IRIS and SST observations

L.H.M. Rouppe van der Voort^{1,2}, B. De Pontieu^{3,1,2}, M. Carlsson^{1,2}, J. de la Cruz Rodríguez⁴, S. Bose^{1,2}, G. Chintzoglou^{3,5}, A. Drews^{1,2}, C. Froment^{1,2,6}, M. Gošić^{3,7}, D.R. Graham^{3,7}, V.H. Hansteen^{1,2,3,7}, V.M.J. Henriques^{1,2}, S. Jafarzadeh^{1,2}, J. Joshi^{1,2}, L. Kleint^{8,9}, P. Kohutova^{1,2}, T. Leifsen^{1,2}, J. Martínez-Sykora^{3,7,1,2}, D. Nóbrega-Siverio^{1,2}, A. Ortiz^{1,2}, T.M.D. Pereira^{1,2}, A. Popovas^{1,2}, C. Quintero Noda^{1,2}, A. Sainz Dalda^{3,7,10}, G.B. Scharmer⁴, D. Schmit¹¹, E. Scullion^{12,1}, H. Skogsrud¹, M. Szydlarski^{1,2}, R. Timmons³, G.J.M. Vissers^{4,1}, M.M. Woods^{3,7}, and P. Zacharias¹

¹ Institute of Theoretical Astrophysics, University of Oslo, P.O. Box 1029 Blindern, N-0315 Oslo, Norway

² Rosseland Centre for Solar Physics, University of Oslo, P.O. Box 1029 Blindern, N-0315 Oslo, Norway

³ Lockheed Martin Solar & Astrophysics Laboratory, 3251 Hanover St., Palo Alto, CA 94304, USA

⁴ Institute for Solar Physics, Dept. of Astronomy, Stockholm University, AlbaNova University Centre, 10691, Stockholm, Sweden

⁵ University Corporation for Atmospheric Research, Boulder, CO 80307-3000, USA

⁶ LPC2E, CNRS and University of Orléans, 3A avenue de la Recherche Scientifique, Orléans, France

⁷ Bay Area Environmental Research Institute, NASA Research Park, Moffett Field, CA 94035, USA

⁸ University of Applied Sciences and Arts Northwestern Switzerland, Bahnhofstrasse 6, 5210 Windisch, Switzerland

⁹ Leibniz-Institut für Sonnenphysik (KIS), Schöneckstrasse 6, D-79104 Freiburg, Germany

¹⁰ Stanford University, HEPL, 466 Via Ortega, Stanford, CA 94305-4085

¹¹ Catholic University of America, Washington, DC 20064, USA; NASA Goddard Space Flight Center, Greenbelt, MD 20771, USA

¹² Department of Mathematics, Physics and Electrical Engineering, Northumbria University, Newcastle upon Tyne NE1 8ST, UK

July 13, 2022

ABSTRACT

NASA's Interface Region Imaging Spectrograph (IRIS) provides high resolution observations of the solar atmosphere through UV spectroscopy and imaging. Since the launch of IRIS in June 2013, we have conducted systematic observation campaigns in coordination with the Swedish 1-m Solar Telescope (SST) on La Palma. The SST provides complementary high-resolution observations of the photosphere and chromosphere. The SST observations include spectro-polarimetric imaging in photospheric Fe I lines and spectrally-resolved imaging in the chromospheric Ca II 8542Å, H α , and Ca II K lines. We present a database of co-aligned IRIS and SST datasets that is open for analysis to the scientific community. The database covers a variety of targets including active regions, sunspots, plage, quiet Sun, and coronal holes.

Key words. Sun: photosphere – Sun: chromosphere – Sun: transition region

1. Introduction

The solar atmosphere is a very dynamic region where fundamental physical processes take place at small spatial scales and short dynamical time scales, often leading to rapid changes in thermodynamic state of the plasma. Resolving these processes in observations requires high resolution in the combined spatial, temporal and spectral domains. Further, the combination of multiple spectral diagnostics, preferably with sensitivity to line formation conditions that cover a large range in temperatures, densities, and magnetic field topologies, are of fundamental importance for advancing our understanding of the solar atmosphere. The simultaneous acquisition of vastly different spectral diagnostics is possible through coordinated observations between space-borne and ground-based observing facilities. Telescopes in space provide unique access to the short wavelength regime with seeing-free diagnostics of the chromosphere, transition region and corona. Ground-based telescopes allow high resolution in photospheric

and chromospheric diagnostics, as well as high sensitivity polarimetric measurements of the magnetic field with instrumentation that can be far more complex than in space, and that is not limited by data transfer rates. Coordinated observations, therefore, strongly enhance the potential to unravel connections in solar atmosphere that span from the photosphere, through the chromosphere and transition region to the corona.

The Interface Region Imaging Spectrograph (IRIS, [De Pontieu et al. 2014b](#)), a NASA Small Explorer (SMEX) satellite, was launched on June 27, 2013. It combines high resolution in the spatial (0'3–0'4), temporal (down to 1 s) and spectral domains (velocity determination down to 1 km/s). Spectral diagnostics include the Mg II h & k resonance lines (chromosphere), the C II lines at 1335 Å (upper chromosphere and transition region), and the Si IV lines at 1400Å (transition region). Further, the (weaker) O IV lines around 1400Å and Fe XII 1349Å and Fe XXI 1354Å lines provide diagnostics on the corona and high-energy flares.

Slit-jaw imaging in the Mg II k core, Mg II h wing, C II, and Si IV lines provides valuable context information.

IRIS offers considerable flexibility in its observing configuration and for example allows a wide variety in area coverage (i.e., field-of-view (FOV) size), temporal cadence, and choice of spectral diagnostics. Target selection is organised through a system with relatively short communication lines and allows for effective coordination with ground-based telescopes and other observing facilities. This has opened possibilities to expand on IRIS' rich arsenal of spectral diagnostics, e.g. by adding photospheric and chromospheric spectropolarimetry and high-resolution imaging in various spectral lines at and around the area covered by the IRIS spectrograph slit.

Shortly after IRIS was launched, scientists from the University of Oslo and from the Lockheed Martin Solar and Astrophysics Laboratory (LMSAL) started organising coordinated observing campaigns with the Swedish 1-m Solar Telescope (SST, [Scharmer et al. 2003a](#)) on La Palma. Every year, four campaigns – typically 2 weeks each – are conducted during the SST observing season (April – October). The SST is capable of providing high-quality time series of spectrally resolved photospheric and chromospheric diagnostics that under excellent seeing conditions reach the diffraction limit of $<0''.1$ over the full arcmin² FOV. Furthermore, the versatile CRISP instrument can provide spectro-polarimetric data that enable measurement of the magnetic field topology. In addition, the tunable filter system CHROMIS can simultaneously provide narrowband filtergrams at several wavelengths in the core of the Ca II K line.

In this paper, we describe the public release of co-aligned IRIS and SST data. At first, the public release is restricted to data products that share the same plate scale as IRIS ($0''.17$, for easier data analysis). This pixel scale implies that the spatial resolution of the SST data is degraded. The release of the corresponding full spatial resolution SST data is planned for future data releases.

2. Observations and data processing

2.1. IRIS

The IRIS telescope design and instrumentation are described in [De Pontieu et al. \(2014b\)](#). IRIS acquires spectra in 3 spectral regions, in the far UV from 1332 to 1358 Å (FUV1) and from 1389 to 1407 Å (FUV2), and in the near UV from 2783 to 2834 Å (NUV). The FUV1 region is dominated by the C II lines at 1334 and 1335 Å that are formed in the upper chromosphere ([Rathore et al. 2015a,b](#)), the FUV2 region is dominated by the Si IV lines at 1394 and 1403 Å that are formed in the transition region. The NUV region is dominated by the chromospheric Mg II h and k lines ([Leenaarts et al. 2013a,b](#)), and further hosts the upper photospheric/lower chromospheric Mg II triplet lines ([Pereira et al. 2015](#)) and a large number of (upper) photospheric blends in the strong Mg II wings ([Pereira et al. 2013](#)).

The $0''.33$ wide spectrograph slit has a length of $175''$ and can be displaced with respect to the solar surface to build up a raster that samples an area up to $130'' \times 175''$. There are several choices of step sizes between consecutive slit positions: dense, continuous sampling with $0''.35$ steps, sparse sampling with $1''$ steps, or coarse sampling with $2''$ steps. Alternatively, the spectrograph can record data in a sit-and-stare mode, where the slit does not move and stays at a fixed location (with or without tracking for solar rotation).

IRIS can take slit-jaw images (SJI) with different filters to provide context around the spectrograph slit. The four science SJI channels are: SJI 2796, centered on Mg II k (4 Å bandpass);

SJI 2832, centered at 2830 Å in the Mg II h wing (4 Å bandpass); SJI 1330, centered at 1340 Å and dominated by the C II lines (55 Å bandpass); and SJI 1400, centered at 1390 Å and dominated by the Si IV lines (55 Å bandpass). SJI images from different channels are recorded sequentially and have the same exposure time as the spectrograms recorded with the spectrograph.

Various choices can be made to reduce the data volume in order to fit within the daily limits of data transfer from the spacecraft to ground stations. For each spectral line of interest, the wavelength range can be selected to limit the data transferred, or the spatial extent of the raster can be limited by transferring only data from a reduced part of the slit. Other measures to reduce data transfer are compression, data binning (spatially and/or spectrally), and omitting one or several SJI channels (most often, SJI 2832 is omitted, although this is often done to improve the cadence of the other SJI channels).

Taken together, the various possible choices in raster step size, number of slit positions, slit length, SJI channel selection, exposure time, spatial and spectral binning, compression, and spectral line selection (line lists) constitute a considerable number of possible observing programs. These programs are identified by a unique number, the OBS number (or OBSID, for more details see, [De Pontieu et al. 2014b](#)). The OBSID, together with the observing date and start time, constitute a unique identifier for each dataset (see first 3 columns in Table 1)

2.2. SST

The SST telescope design and its main optical elements are described in [Scharmer et al. \(2003a\)](#). A description of upgrades of optical components and instrumentation, as well as a thorough evaluation of optical performance is provided by [Scharmer et al. \(2019\)](#). An adaptive optics system is fully integrated in the optical system ([Scharmer et al. 2003b](#)) and was upgraded with a 85-electrode deformable mirror operating at 2 kHz in 2013. A dichroic beamsplitter divides the beam on the optical table into a red ($> 500 \text{ nm}$) and a blue beam. Both beams are equipped with tunable filter instruments: the CRISP imaging spectropolarimeter ([Scharmer et al. 2008](#)) on the red beam, and the CHROMIS imaging spectrometer on the blue beam. Both CRISP and CHROMIS are dual Fabry-Pérot filtergraph systems based on the design by [Scharmer \(2006\)](#) and are capable of fast wavelength sampling of spectral lines. Before the installation of CHROMIS in September 2016, the blue beam was equipped with a number of interference filters, including a FWHM= 10 Å wide filter for photospheric imaging at 3954 Å , and a FWHM= 1 Å wide filter centered on the Ca II H line core at $\lambda = 3968 \text{ Å}$ (see [Löfdahl et al. 2011](#)). CRISP has a pair of liquid crystals that allows measurements of circular and linear polarisation in for example the photospheric Fe I 6173 Å, Fe I 6301 Å, and Fe I 6302 Å lines, and the chromospheric Ca II 8542 Å line.

CRISP has a plate scale of $0''.058$ per pixel and the SST diffraction limit $\lambda/D = 0''.14$ at the wavelength of H α (with the telescope aperture diameter $D=0.97 \text{ m}$). The transmission profile of CRISP has FWHM= 60 mÅ at the wavelength of H α . CHROMIS has a plate scale of $0''.038$ per pixel and the SST diffraction limit is $0''.08$ at the wavelength of Ca II K. The transmission profile of CHROMIS has FWHM $\approx 120 \text{ mÅ}$ at the wavelength of Ca II K. The FOV of CRISP and CHROMIS is approximately $1' \times 1'$. Note that sunlight from the SST is split by a dichroic beam splitter such that CRISP and CHROMIS can

operate independently and in parallel, without reducing the efficiency of either instrument.

Image restoration by means of the multi-object multi-frame blind deconvolution (MOMFBD, Löfdahl 2002; van Noort et al. 2005) method is applied to all data to enhance image quality over the full FOV. MOMFBD restoration is integrated in the CRISP and CHROMIS data processing pipelines (de la Cruz Rodríguez et al. 2015; Löfdahl et al. 2018). These pipelines include the method described by Henriques (2012) for consistency between sequentially recorded liquid crystal states and wavelengths, with destretching performed as in Shine et al. (1994). The CRISP and CHROMIS instruments include auxiliary wide-band (WB) systems which are essential as anchor channels in MOMFBD restoration. Furthermore, they provide photospheric reference channels that facilitate precise co-alignment between CRISP and CHROMIS (or blue beam filters before 2016) data, or co-alignment with data from IRIS and the Solar Dynamic Observatory (SDO, Lemen et al. 2012).

2.3. SST observing programs

The SST observing programs vary from campaign to campaign, often also during campaigns depending on the target and science goals. Common to all datasets in the database is the inclusion of a chromospheric line, $H\alpha$ or $\text{Ca II } 8542 \text{ \AA}$, and often both. In order to keep the temporal cadence below 20 s, the $\text{Ca II } 8542 \text{ \AA}$ observations were most often in non-polarimetric mode.

During the 2013 and 2014 observing seasons, photospheric spectro-polarimetry was limited to one single position in the blue wing of the $\text{Fe I } 6302 \text{ \AA}$ line. The Stokes V maps serve as effective locators of the strongest magnetic field regions and polarity indicators.

During later campaigns, spectral sampling of photospheric Fe I lines was extended. These observations were subjected to a fast and robust pixel-to-pixel Milne-Eddington inversion procedure. The parallel C++ implementation (de la Cruz Rodríguez 2019) is based upon the analytical intensity derivatives described by Orozco Suárez & Del Toro Iniesta (2007) and an efficient Levenberg-Marquardt algorithm that is described in de la Cruz Rodríguez et al. (2019).

Example line of sight magnetic field strength (B_{LOS}) maps from $\text{Fe I } 6173 \text{ \AA}$ inversions are shown in Fig. 1, for observing dates 2015-Jun-26 and 2015-Sep-17. The database contains maps of B_{LOS} , plane of the sky magnetic field strength B_{perp} , and LOS velocity from these ME inversions.

2.4. IRIS and SST co-alignment

For the co-alignment of the IRIS and SST data, we employ cross-correlation of image pairs that are morphologically as similar as possible. Most often, the SJI 2796 and $\text{Ca II } 8542 \text{ \AA}$ wing (at 0.8 – 1.2 \AA offset from line core) or Ca II K wing prove to show similar enough scenes to give satisfying results. This is particularly true for more quiet regions with the characteristic mesh-like pattern from acoustic shocks and the surrounding network of high contrast bright regions. For active regions with enhanced flaring activity or large sunspots, the SJI 2796 and $\text{Ca II } 8542 \text{ \AA}$ wing pair can have more dissimilar scenes and therefore the co-alignment can be less reliable.

The combination SJI 2832 with CRISP WB or $H\alpha$ far wing gives excellent co-alignment results since both channels show pure photospheric scenes. However, SJI 2832 is not always se-

lected for the IRIS observing programs to limit the data rate and improve the cadence of the other SJI channels.

Before cross-correlation, the plate scales between image pairs are matched. Offsets are then determined by cross-correlation over a subfield of the common FOV of image pairs that are closest in time. Examples of such subfields are outlined by white rectangles in Fig. 1. The raw offsets are then smoothed with a temporal window to account for jitter due to noise. The offsets that are applied to the data are interpolated to the relevant time grid of the particular diagnostic.

The precision of the alignment is limited by a number of factors. Formation height differences between the diagnostics used for cross-correlation may introduce a systematic offset that is difficult to account for. This is probably of limited concern for cross-correlation between photospheric diagnostics involving SJI 2832, but more uncertain between SJI 2796 and the $\text{Ca II } 8542$ wing. The systematic offset may be higher for oblique observing angles towards the limb and may also depend on the type of target (for example active regions with flaring activity that appears less prominent in the $\text{Ca II } 8542$ wing than in Mg II k core). Further, varying seeing conditions at the SST inevitably lead to image distortions that cannot be fully accounted for in post-processing. We estimate that the co-alignment can be as good as smaller than the IRIS pixel size of $0''.17$ (in the case of SST data taken under excellent conditions and closely matching diagnostic pairs in the cross-correlation). However, we also see local offsets due to image warping that can be as large as ~ 2 IRIS pixels. These local offsets vary in magnitude proportionally with the seeing conditions.

For the current release of data to the database, the IRIS data is kept as reference. This means that the SST data is down-scaled to the IRIS plate scale (for CRISP with a factor 2.9, for CHROMIS with a factor 4.4), rotated and clipped to match the IRIS FOV and orientation, and clipped in time to match the IRIS observation duration. We have also applied the reverse approach, keeping at least the SST data at its superior spatial resolution for analysis in earlier publications. These types of data products are considered for future data releases but we note that the quality control is a laborious effort, partly due to the alignment uncertainties outlined above.

3. Data in the database

Table 1 gives an overview of various parameters that characterise data sets in the public database. There is a variety of targets including quiet Sun, coronal holes, enhanced network, active regions with and without sunspots, and plage.

The data can be accessed through the database accessible through the public web portal at the IRIS web pages at LMSAL¹. The data products that are publicly released are FITS files in so-called IRIS level 3 format. Level 3 data are data cubes that are a recast of the standard IRIS level 2 data files. Level 2 data are the science-ready data files that have been processed to include corrections for dark current and flat field, geometric distortions and wavelength calibration. The level 3 are 4-dimensional data cubes with (x, y, λ, t) -axes with the spatial x -axis along the raster slit positions, the spatial y -axis along the spectrograph slit, the λ -axis along the wavelength dimension, and t the temporal axis.

The level 3 data cubes in the database can be readily accessed with CRISPEx (Vissers & Roupe van der Voort 2012; Löfdahl et al. 2018), a graphical user interface written in the Interactive

¹ <https://iris.lmsal.com/search/>

Data Language (IDL). It allows side-by-side browsing and basic time-series analysis of the IRIS rasters, SJIs and CRISP or CHROMIS data. CRISPEX is distributed as part of the IRIS package in SolarSoft IDL and can also be downloaded² separately, however it requires SolarSoft for full functionality when inspecting the IRIS-SST data. Tutorials for its use are available online.^{2,3}

Acknowledgements. This paper is dedicated to Ted Tarbell who passed away in April 2019. Ted was the leader of the LMSAL SVST/SST campaigns since the 1980s through the 2000s and participated with great enthusiasm in the LMSAL campaigns in 2013 and 2014. Ted was a great friend and an inspiring mentor to his junior colleagues. The Swedish 1-m Solar Telescope is operated on the island of La Palma by the Institute for Solar Physics of Stockholm University in the Spanish Observatorio del Roque de los Muchachos of the Instituto de Astrofísica de Canarias. The Institute for Solar Physics is supported by a grant for research infrastructures of national importance from the Swedish Research Council (registration number 2017-00625). IRIS is a NASA small explorer mission developed and operated by LMSAL with mission operations executed at NASA Ames Research Center and major contributions to downlink communications funded by ESA and the Norwegian Space Centre. We thank the following people for their assistance at the SST: Jack Carlyle, Tiffany Chamandy, Henrik Eklund, Thomas Golding, Chris Hoffmann, Charalambos Kanella, Ingrid Marie Kjelseth, and Bhavna Rathore. We further acknowledge excellent support at the SST by Pit Sütterlin. We are also grateful to the IRIS planners for the IRIS-SST coordination. This research is supported by the Research Council of Norway, project number 250810, and through its Centres of Excellence scheme, project number 262622. BDP and colleagues at LMSAL and BAERI acknowledge support from NASA contract NNG09FA40C (IRIS). JdICR is supported by grants from the Swedish Research Council (2015-03994), the Swedish National Space Board (128/15) and the Swedish Civil Contingencies Agency (MSB). This project has received funding from the European Research Council (ERC) under the European Union's Horizon 2020 research and innovation programme (SUNMAG, grant agreement 759548). VMJH and SJ receive funding from the European Research Council (ERC) under the European Union's Horizon 2020 research and innovation programme (grant agreement No. 682462). JMS is supported by NASA grants NNX17AD33G, 80NSSC18K1285, and NSF grant AST1714955. GV is supported by a grant from the Swedish Civil Contingencies Agency (MSB). CF acknowledges funding from CNES. We made much use of NASA's Astrophysics Data System Bibliographic Services.

References

- Bose, S., Henriques, V. M. J., Rouppe van der Voort, L., & Pereira, T. M. D. 2019, *A&A*, 627, A46
- de la Cruz Rodríguez, J. 2019, *A&A*, 631, A153
- de la Cruz Rodríguez, J., Leenaarts, J., Danilovic, S., & Uitenbroek, H. 2019, *A&A*, 623, A74
- de la Cruz Rodríguez, J., Löfdahl, M. G., Sütterlin, P., Hillberg, T., & Rouppe van der Voort, L. 2015, *A&A*, 573, A40
- De Pontieu, B., Rouppe van der Voort, L., McIntosh, S. W., et al. 2014a, *Science*, 346, 1255732
- De Pontieu, B., Title, A. M., Lemen, J. R., et al. 2014b, *Sol. Phys.*, 289, 2733
- Draws, A. & Rouppe van der Voort, L. 2020, arXiv e-prints, [arXiv:2005.02608](https://arxiv.org/abs/2005.02608)
- Henriques, V. M. J. 2012, *A&A*, 548, A114
- Leenaarts, J., Pereira, T. M. D., Carlsson, M., Uitenbroek, H., & De Pontieu, B. 2013a, *ApJ*, 772, 89
- Leenaarts, J., Pereira, T. M. D., Carlsson, M., Uitenbroek, H., & De Pontieu, B. 2013b, *ApJ*, 772, 90
- Lemen, J. R., Title, A. M., Akin, D. J., et al. 2012, *Sol. Phys.*, 275, 17
- Löfdahl, M. G. 2002, in *Society of Photo-Optical Instrumentation Engineers (SPIE) Conference Series*, Vol. 4792, Proc. SPIE, ed. P. J. Bones, M. A. Fiddy, & R. P. Millane, 146–155
- Löfdahl, M. G., Henriques, V. M. J., & Kiselman, D. 2011, *A&A*, 533, A82
- Löfdahl, M. G., Hillberg, T., de la Cruz Rodríguez, J., et al. 2018, ArXiv e-prints 1804.03030
- Martínez-Sykora, J., De Pontieu, B., Hansteen, V. H., et al. 2017, *Science*, 356, 1269
- Martínez-Sykora, J., Rouppe van der Voort, L., Carlsson, M., et al. 2015, *ApJ*, 803, 44
- Nóbrega-Siverio, D., Martínez-Sykora, J., Moreno-Insartís, F., & Rouppe van der Voort, L. 2017, *ApJ*, 850, 153

- Orozco Suárez, D. & Del Toro Iniesta, J. C. 2007, *A&A*, 462, 1137
- Ortiz, A., Hansteen, V. H., Nóbrega-Siverio, D., & van der Voort, L. R. 2020, *A&A*, 633, A58
- Pereira, T. M. D., Carlsson, M., De Pontieu, B., & Hansteen, V. 2015, *ApJ*, 806, 14
- Pereira, T. M. D., Leenaarts, J., De Pontieu, B., Carlsson, M., & Uitenbroek, H. 2013, *ApJ*, 778, 143
- Rathore, B., Carlsson, M., Leenaarts, J., & De Pontieu, B. 2015a, *ApJ*, 811, 81
- Rathore, B., Pereira, T. M. D., Carlsson, M., & De Pontieu, B. 2015b, *ApJ*, 814, 70
- Rouppe van der Voort, L., De Pontieu, B., Pereira, T. M. D., Carlsson, M., & Hansteen, V. 2015, *ApJ*, 799, L3
- Rouppe van der Voort, L., De Pontieu, B., Scharmer, G. B., et al. 2017, *ApJ*, 851, L6
- Rouppe van der Voort, L. H. M., Rutten, R. J., & Vissers, G. J. M. 2016, *A&A*, 592, A100
- Rutten, R. J. & Rouppe van der Voort, L. H. M. 2017, *A&A*, 597, A138
- Scharmer, G. B. 2006, *A&A*, 447, 1111
- Scharmer, G. B., Bjelksjö, K., Korhonen, T. K., Lindberg, B., & Petterson, B. 2003a, in *Proc. SPIE*, Vol. 4853, Innovative Telescopes and Instrumentation for Solar Astrophysics, ed. S. L. Keil & S. V. Avakyan, 341–350
- Scharmer, G. B., Dettori, P. M., Löfdahl, M. G., & Shand, M. 2003b, in *Proc. SPIE*, Vol. 4853, Innovative Telescopes and Instrumentation for Solar Astrophysics, ed. S. L. Keil & S. V. Avakyan, 370–380
- Scharmer, G. B., Löfdahl, M. G., Sliepen, G., & de la Cruz Rodríguez, J. 2019, *A&A*, 626, A55
- Scharmer, G. B., Narayan, G., Hillberg, T., et al. 2008, *ApJ*, 689, L69
- Shine, R. A., Title, A. M., Tarbell, T. D., et al. 1994, *ApJ*, 430, 413
- van Noort, M., Rouppe van der Voort, L., & Löfdahl, M. G. 2005, *Sol. Phys.*, 228, 191
- Vissers, G. & Rouppe van der Voort, L. 2012, *ApJ*, 750, 22
- Vissers, G. J. M., de la Cruz Rodríguez, J., Libbrecht, T., et al. 2019, *A&A*, 627, A101
- Vissers, G. J. M., Rouppe van der Voort, L. H. M., & Carlsson, M. 2015a, *ApJ*, 811, L33
- Vissers, G. J. M., Rouppe van der Voort, L. H. M., Rutten, R. J., Carlsson, M., & De Pontieu, B. 2015b, *ApJ*, 812, 11

² <http://folk.uio.no/gregal/crispex>

³ <https://iris.lmsal.com/tutorials.html>

Table 1. Overview of the datasets available in the database.

Date ^a	Time ^b	OBSID ^c	<i>n</i>	type	Raster ^d FOV [']	Cad. [s]	Target ^e	Pointing (solar X, Y) ["]	μ^f	Overlap ^g	SST diagnostics ^h	Cad. [s]	Ref. ⁱ
20130906	081104	4003004168	4	sparse	3 × 50	11.5	AR, S	773, 128	0.57	00:45:30	H α	5.5	5
20130910	080943	4003007165	2	sparse	1 × 50	10.0	AR	-173, -189	0.96	01:12:54	H α	5.5	2
20130922	073430	4004007147	1	sit	0.3 × 60	4.2	CH	551, 295	0.77	02:02:16	H α , Ca 8542, Fe 6302	10.9	1, 2, 3
20140614	072931	3820256197	96	dense	31 × 175	516	AR	235, 277	0.92	00:51:32	H α , Ca 8542, Fe 6302	11.4	5
20140621	073138	3820259497	96	dense	31 × 175	908	QS	-201, 258	0.94	01:43:41	H α , Ca 8542, Fe 6302	11.5	7
20140905	080604	3820255167	4	sparse	3 × 60	13.2	AR, S	702, -304	0.59	01:53:00	H α , Ca 8542, Fe 6302	11.6	4
20140906	080537	3820255167	4	sparse	3 × 60	13.2	AR, S	819, -281	0.41	02:01:02	H α , Ca 8542, Fe 6302	11.6	4
20150626	070915	3630105426	8	dense	2.3 × 60	25	QS	-422, -260	0.85	02:31:06	H α , Ca 8542, Fe 6173	16.1	8
20150917	073915	3630104144	32	dense	10.2 × 60	99	QS	725, 38	0.65	00:24:46	H α , Ca 8542, Fe 6173	24.1	6
20160429	074917	3620106129	8	sparse	7 × 60	41	AR, S	634, 18	0.74	01:29:50	H α , Ca 8542	20	12, 14
20160903	074446	3625503135	16	dense	5 × 60	21	AR	-561, 44	0.81	02:14:30	H α , Ca 8542	20	9, 13
										00:34:20	Ca II K	13	10, 11
20160904	074446	3625503135	16	dense	5 × 60	21	AR	-374, 27	0.91	01:09:26	H α , Ca 8542	20	13
										00:34:04	Ca II K	22	10, 11

Notes. ^(a) Observing date in format year, month, day^(b) Starting time (UT) of observations in format hour, min, s^(c) The OBSID number encodes the IRIS observing configuration in a unique number (see Tables 12–14 in De Pontieu et al. 2014b). The combination $\langle Date \rangle \langle Time \rangle \langle OBSID \rangle$ constitutes a unique identifier to the dataset.^(d) The IRIS spectrograph slit covers a region on the Sun through a raster of n slit positions, with a separation of type: dense (0'32), sparse (1''), or coarse (2''). Raster type sit is the “sit-and-stare” mode for which the slit remains fixed at one location. The area covered is shown in the FOV column, and the temporal cadence in the Cad. column.^(e) Target: AR: active region, QS: quiet Sun, CH: coronal hole, F: flare, S: sunspot ^(f) $\mu = \cos \theta$ with θ the observing angle.^(g) Duration of overlap of SST observations with IRIS. Note that CRISP and CHROMIS are operated independently and can have different overlap times.^(h) Spectral lines observed with SST. ⁽ⁱ⁾ Cadence of the SST observations. ^(j) References to publications based on these data sets: 1: De Pontieu et al. (2014a), 2: Rouppe van der Voort et al. (2015), 3: Martínez-Sykora et al. (2015), 4: Vissers et al. (2015a), 5: Vissers et al. (2015b), 6: Rouppe van der Voort et al. (2016) 7: Rutten & Rouppe van der Voort (2017), 8: Martínez-Sykora et al. (2017), 9: Nóbrega-Siverio et al. (2017), 10: Rouppe van der Voort et al. (2017), 11: Vissers et al. (2019), 12: Bose et al. (2019), 13: Ortiz et al. (2020) 14: Drews & Rouppe van der Voort (2020)

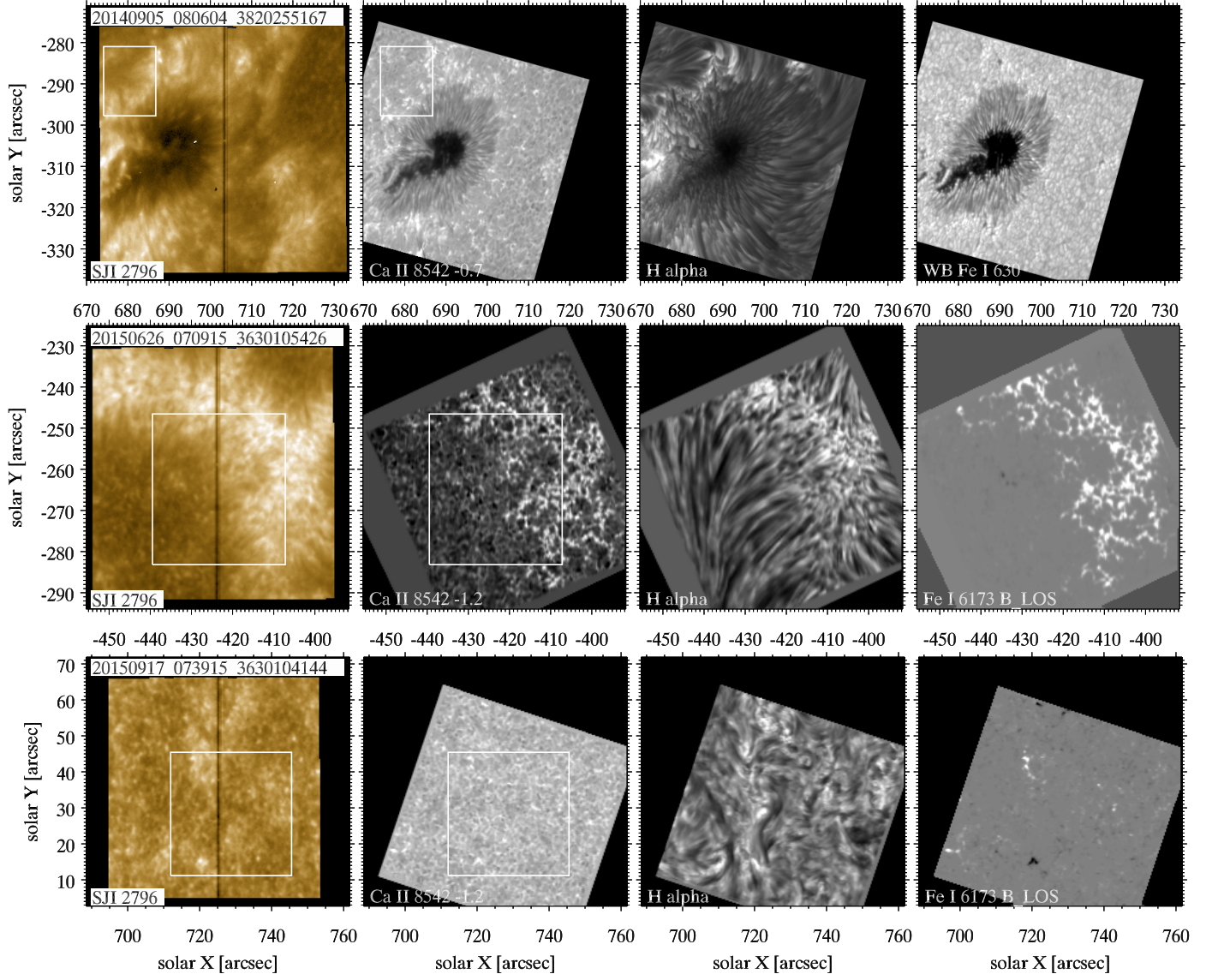


Fig. 1. Sample images from three different datasets. Each row shows four different diagnostics. The first two images on each row show the channel pairs that were used for IRIS/SST co-alignment, the area outlined by the white rectangle marks the region used for cross-correlation to determine offsets. The SST images are down scaled to IRIS plate scale.